Redox-active ruthenium-organic polyhedra with tunable surface functionality and porosities

Fuerkaiti Tayier,[a,b] Javier Troyano,[a,c,d] Shun Tokuda,[a,b] Zaoming Wang,[a] Masa-aki Haga[e] and Shuhei Furukawa[a,b*]

[a]Institute for Integrated Cell-Material Sciences (iCeMS), Kyoto University, Yoshida, Sakyo-ku, Kyoto 606-8501, Japan

[b]Department of Synthetic Chemistry and Biological Chemistry, Graduate School of Engineering, Kyoto University, Katsura, Nishikyo-ku, Kyoto 615-8510, Japan

[c]Department of Inorganic Chemistry, Autonomous University of Madrid, 28049 Madrid, Spain

[d]Institute for Advanced Research in Chemical Sciences (IAdChem), Autonomous University of Madrid, 28049 Madrid, Spain

[e]Research & Development Initiative, Chuo University, 1-13-27 Kasuga, Bunkyo-ku, Tokyo 112-8551, Japan

KEYWORDS: dinuclear ruthenium paddlewheel, metal-organic polyhedra, gas sorption, electrochemistry.

ABSTRACT: Dinuclear ruthenium paddlewheel complexes exhibit high structural stability against redox reactions. The use of these chemical motifs for the construction of Ru-based metal-organic polyhedral (RuMOPs) provides a route for redox-active porous materials. However, there are few studies on the synthesis and characterization of RuMOPs due to the difficulty of controlling the assembling process via the ligand-exchange reaction of equatorial acetates of the diruthenium tetraacetate precursors with dicarboxylic acid ligands. In this study, we synthesized three novel cuboctahedral RuMOPs based on the Ru_2(II/III)-paddlewheel units with different alkyl functionalizations on the benzene-1,3-dicarboxylate moieties. We evaluated the effect of the external functionalization on the molecular packing and the porous and redox properties. The electrochemical measurements revealed the multi-electron transferred redox process where the electron donating/withdrawing nature of the functional groups allows the control of the redox behavior.

Introduction

Redox-active property refers to the ability of a substance to undergo the transfer of electrons between different chemical species. Such property has been widely introduced into supramolecular structures by assembling multiple redox sites towards the use of multi-electron transfer[1,2] for high energy density batteries,[3,4] electrocatalysis,[5] electrochromism[6,7] and mimicking intricate biological processes.[8] The multi-electron transfer process is strongly correlated to supramolecular structures and geometries, in which the number of redox-active moieties can be changed by altering or modifying the structures of relevant building blocks.[2]

Metal-organic polyhedra (MOPs), alternatively known as metal-organic cages (MOCs), are a class of supramolecular structures that are discrete cage-like porous molecules assembled from organic ligands and metal nodes.[9] MOPs have gained significant interest over the past decade for gas storage[10], molecular separation[11] and drug delivery[12] due to their designable intrinsic void structures. The designability of MOPs enables the incorporation of functional sites/groups into the metal nodes or organic ligands via pre-designed or post-synthetic approaches,[13,14,15] leading to photo-active,[16] guest-responsive,[17] and redox-active properties.[18] Despite the fact that the confined space of redox-active MOPs offers promising efficiency for catalytic reactions, the studies on redox-active MOPs are still limited since their construction requires structural integrity against redox reactions.

Based on the few available cases of redox-active MOPs, the design strategy involves the incorporation of redox-responsive moieties, either metal nodes or organic ligands, into the MOPs structure. The example of organic or metalloligands includes 2,4,6-tri-4-pyridyl-1,3,5-triazine,[16,19,20] or metalloligands with ferrocene,[21] or ruthenium tris(1,10-phenanthroline) moieties.[22] Regarding the redox-active metal node of MOPs, one can select it from a library of redox-active metal complexes, which allows for the choice of various ligand types and the design of the resulting geometry of MOPs. However, MOPs with redox-active metal nodes

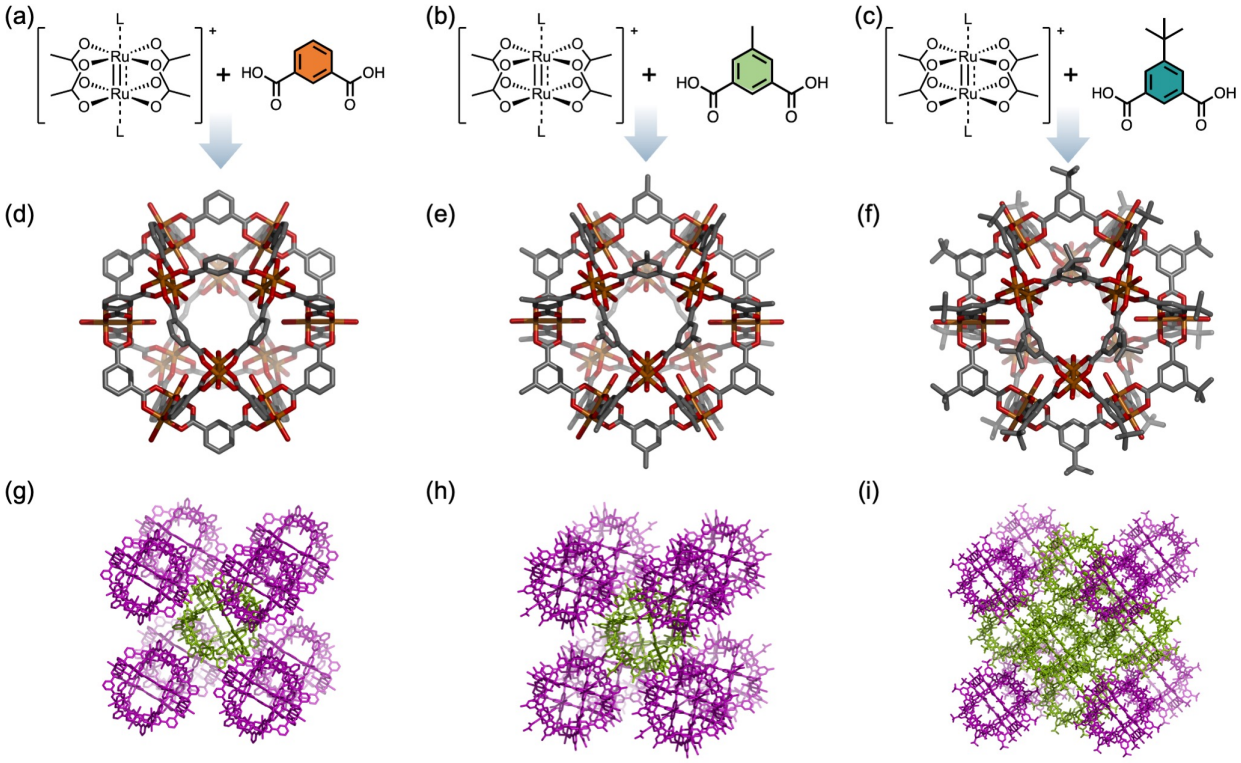

Figure 1. (a) Ru_2(II/III)-paddlewheel, $[Ru_2(OAc)_4]^+$ and organic ligands bdc; (b) $[Ru_2(OAc)_4]^+$ and Me-bdc; (c) $[Ru_2(OAc)_4]^+$ and *t*-Bu-bdc; L represents solvent molecule at the axial position of Ru_2(II/III)-paddlewheel. The counter anions of Ru-paddlewheels were omitted for clarity; the molecular structure of (d) **H-RuMOP**, (e) **Me-RuMOP** and (f) ***t*-Bu-RuMOP**. Hydrogens, axial coordinated solvent molecule of **Me-RuMOP** and disordered atoms of ***t*-Bu-RuMOP** were omitted for clarity. Ru, brown; C, gray; O, red. The arrangement of (g) **H-RuMOP**, (h) **Me-RuMOP** and (i) ***t*-Bu-RuMOP**.

are still in their infancy. To date, only Fe(II), Fe(III), Ni(II) and dinuclear Ru_2-paddlewheels have been used as redox-active metal nodes.[18,23-25] Among them, Ru_2-paddlewheels are the most promising metal nodes for the construction of redox-active MOPs (RuMOPs) because of their two stable redox states of Ru_2(II/II) and Ru_2(II/III) and the structural integrity as RuMOPs to offer the permanent porosity in the solid-state.[10,26]

The first redox-active RuMOPs were reported in 2015.[25] One system is a cuboctahedral $[Ru_2(R\text{-}bdc)_2]_{12}$, in which twelve Ru_2-paddlewheels with twenty-four 5-substituted benzene-1,3-dicarboxylate (R-bdc) are assembled. The other is an octahedral $[Ru_2(Cz)_2]_6$, in which six Ru_2-paddlewheels with twelve 9*H*-carbazole-3,6-dicarboxylate (Cz) are assembled. Regarding their oxidation states, the cuboctahedral $[Ru_2(H\text{-}bdc)_2]_{12}$ has Ru_2(II/II) oxidation state and $[Ru_2(t\text{-}Bu\text{-}bdc)_2Cl]_{12}$ does Ru_2(II/III) oxidation state (H-bdc = benzene-1,3-dicarboxylate, *t*-Bu-bdc = 5-*tert*-butylbenzene-1,3-dicarboxylate). The octahedral RuMOPs were synthesized as $[Ru_2(Cz)_2]_6$ and $[Ru_2(Cz)_2Cl]_6$ with Ru_2(II/II) and Ru_2(II/III) oxidation states, respectively.

Since this first report, there has been a lack of articles presenting novel RuMOP structures with their corresponding redox activity and adsorption properties. Very recently, we reported the synthesis of $[Ru_2(OH\text{-}bdc)_2]_{12}(BF_4)_{12}$ (**OH-RuMOP**; OH-bdc = 5-hydroxybenzene-1,3-dicarboxylate) and focused on its reversible self-gelation property and the porous property in the solid-state (powders and aerogel forms).[26]

In this study, we aim to gain insight into the redox properties of RuMOPs and synthesize three novel redox-active RuMOPs with permanent porosity; **H-RuMOP** ($[Ru_2(H\text{-}bdc)_2]_{12}(BF_4)_{12}$) **Me-RuMOP** ($[Ru_2(Me\text{-}bdc)_2]_{12}(BF_4)_{12}$, Me-bdc = 5-methylbenzene-1,3-dicarboxylate) and ***t*-Bu-RuMOP** ($[Ru_2(t\text{-}Bu\text{-}bdc)_2]_{12}(BF_4)_{12}$,), in addition to the previously reported **OH-RuMOP**. The well-defined molecular structures were determined by the single-crystal X-ray diffraction measurements. The multi-electron transferred redox-active properties, as well as the porous properties, were elucidated by the electrochemical and N_2 sorption measurements, respectively.

Results and discussion

Synthesis and structural characterization of RuMOPs. The high solubility of the dinuclear ruthenium paddlewheel precursor of $[Ru_2(OAc)_4(THF)_2](BF_4)$ (THF = tetrahydrofuran) provides a convenient pathway to synthesize the RuMOPs family. By following the previously reported synthetic protocol,[26] $[Ru_2(OAc)_4(THF)_2](BF_4)$ was dissolved in DMA (DMA = *N*,*N*-dimethylacetamide) with R-bdc (R = H, Me, *t*-Bu), followed by heating at 120 °C in the presence of the base to yield the corresponding single crystals of

three different RuMOPs, named **H-RuMOP**, **Me-RuMOP** and ***t*-Bu-RuMOP**. The crystals were suspended in methanol, and then the aqueous solution of HBF_4 was added. The precipitate obtained by centrifugation was dissolved in DMF (DMF = *N,N*-dimethylformamide) and poured into diethyl ether to obtain yellowish-brown amorphous solids as precipitates. The obtained solids were dried at ambient conditions to yield the dried MOP powders, which are soluble in various organic solvents and were used to conduct all experiments in this study.

Single-crystal X-ray diffraction (SCXRD) analysis showed that **H-RuMOP** and **Me-RuMOP** crystallize in the tetragonal $P4/mnc$ space group (Table S1-S2) and ***t*-Bu-RuMOP** crystallizes in the tetragonal $I4/m$ space group (Table S3). All compounds show a cuboctahedral structure, similar to other $[M_2(bdc)_2]_{12}$ MOPs.[9,13,27,28] The Ru-Ru bond distances in the paddlewheel moieties of **H-RuMOP** (2.2717(13) Å and 2.2741(9) Å), **Me-RuMOP** (2.2802(4) and 2.2800(2) Å) and ***t*-Bu-RuMOP** (2.2691(9) Å and 2.2708(6) Å) are comparable to that of previously reported $Ru_2(CO_2)_4$ paddlewheel-based complexes with the Ru_2(II/III) oxidation state.[29] The cavity diameter of three RuMOPs was approximately 16.7 Å, confirmed by the average distance between the inner Ru atom of opposing diruthenium paddlewheel moiety. The axial site of the diruthenium paddlewheel moiety is most likely terminated by DMA molecules, but it was not possible to model the DMA structure from the crystallographic data due to the severe disorder, so we only added oxygen atoms as the axial site ligands. One exception is the case for **Me-RuMOP**; eight out of twelve external axial sites were terminated by solvent DMA molecules that can be explicitly modeled. The counter anion BF_4^- was not crystallographically identified due to the severe disorder. The MOP diameters were defined by the average distance between the carbon atoms at the 5-position of diagonally located dicarboxylate ligands for **H-RuMOP** (25 Å), the carbon atoms in methyl group for **Me-RuMOP** (28 Å) and the terminal carbon atoms of disordered *tert*-butyl group for ***t*-Bu-RuMOP** (29 Å). These sizes are consistent with the hydrodynamic diameters (2 nm - 3 nm) of these RuMOPs in DMF solution estimated by the dynamic light scattering (DLS) experiments (Figure S1-S3).

The **H-RuMOP** and **Me-RuMOP** are packed in body-centered cubic (bcc) arrangements in the crystal structures. In the case of **H-RuMOP,** all eight triangular windows face the triangular windows of neighboring **H-RuMOP**. **Me-RuMOP** is also packed in a similar bcc arrangement but slightly tilts to adapt to each other due to the presence of methyl groups and coordinated solvent molecules of DMA. By contrast to these two cases, ***t*-Bu-RuMOP** is packed in a face-centered cubic (fcc) arrangement. (Figure S4) When considering the "virtual" unit cell based on the fcc arrangements described in Figure 1i, each cell includes four ***t*-Bu-RuMOP** molecules and four octahedral interstitial pockets. Each face of the octahedral pockets consists of three *tert*-butyl groups from three adjacent ***t*-Bu-RuMOP**. This means that each *tert*-butyl group of ***t*-Bu-RuMOP** interacts with two nearby *tert*-butyl groups from two nearby ***t*-Bu-RuMOP**. As a result, there are twenty-four *tert*-butyl groups per octahedral pocket, corresponding to the number of *tert*-butyl groups from ***t*-Bu-RuMOP**.

Fourier-transform infrared spectroscopy (FT-IR) confirmed the presence of the BF_4^- counter anion. All compounds showed a strong absorption band around 1050 cm^{-1}, corresponding to the stretching vibration of BF_4^- (Figure S5).[30] In addition, the presence of mixed-valence Ru_2(II/III) paddlewheel is evidenced by the separation of the symmetric $\nu_{sym}(CO_2)$ and the asymmetric $\nu_{asym}(CO_2)$ bridging carboxylate stretching vibrational modes, $\Delta\nu = \nu_{asym}(CO_2) - \nu_{sym}(CO_2)$ (Figure S6). The separation values for **H-RuMOP**, **Me-RuMOP** and ***t*-Bu-RuMOP** are 57 cm^{-1}, 55 cm^{-1} and 55 cm^{-1}, respectively, which are the typical $\Delta\nu$ values for reported mixed-valence Ru_2(II/III) paddlewheels.[31] Mixed-valence Ru_2(II/III) paddlewheels are cationic, which results in a positive surface on the RuMOPs. This is supported by ζ-potentials of **H-RuMOP**, **Me-RuMOP** and ***t*-Bu-RuMOP** measured in DMF to be +13.9 mV, +25.0 mV and +44.0 mV, respectively.

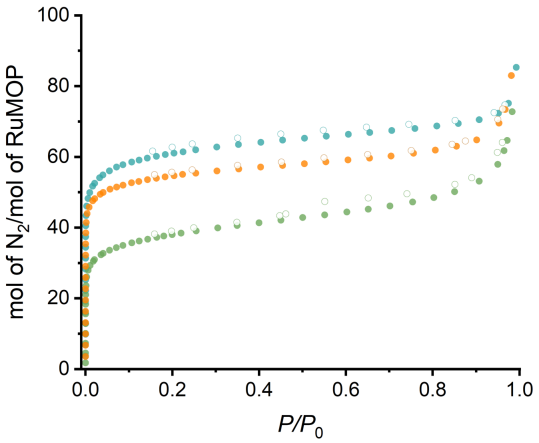

Figure 2. N_2 sorption isotherm at 77 K. **H-RuMOP** (orange), **Me-RuMOP** (green), ***t*-Bu-RuMOP** (cyan).

Porous properties of RuMOPs. Thanks to the thermal stability of **H-RuMOP**, **Me-RuMOP** and ***t*-Bu-RuMOP** as evidenced by the thermogravimetric analysis Figures S7-S9, they withstand the activation process at 120 °C under vacuum, enabling the study of their porosity through gas sorption measurements. The powder X-ray diffraction (PXRD) experiments showed the amorphization of all the samples after the activation; however, only ***t*-Bu-RuMOP** kept the partial crystallinity (Figures S10-S12). The nitrogen sorption isotherms for all compounds were measured at 77 K and are displayed in the mole of N_2 per mole of RuMOP in Figure 2 (the plot in $cm^3\ g^{-1}$ (STP) is shown in Figure S13). All RuMOP samples displayed a sharp uptake of N_2 at the low-pressure region, demonstrating the microporous nature of the materials and confirming the permanent porosity of the RuMOPs (159, 103 and 150 $cm^3\ g^{-1}$ for **H-RuMOP, Me-RuMOP** and ***t*-Bu-RuMOP**, respectively, at P/P_o = 0.1). This suggests that the internal cavity of MOPs remains accessible, even after the rearrangement of MOPs upon

activation. The ***t*-Bu-RuMOP** exhibits a higher uptake than **H-RuMOP** and **Me-RuMOP**. Such results can be attributed to the maintained crystallinity of ***t*-Bu-RuMOP** after activation[32] and the accessible extrinsic porosity benefits from the packing of ***t*-Bu-RuMOP**. The similar effect of functional groups on the resulting porosities was previously discussed by Eric D. Bloch,[33] who reported the influence of the bulkiness of the substituents on the extrinsic porosity between MOPs. The BET surface area was calculated by the BETSI program[34] to be 639, 406 and 594 $m^2 g^{-1}$ for **H-RuMOP**, **Me-RuMOP** and ***t*-Bu-RuMOP** (Figure S14-S16), respectively. These values are relatively smaller than those estimated for the cuboctahedral analogues[35] most likely because some voids are occupied by the counter anion BF_4^- for the RuMOPs.

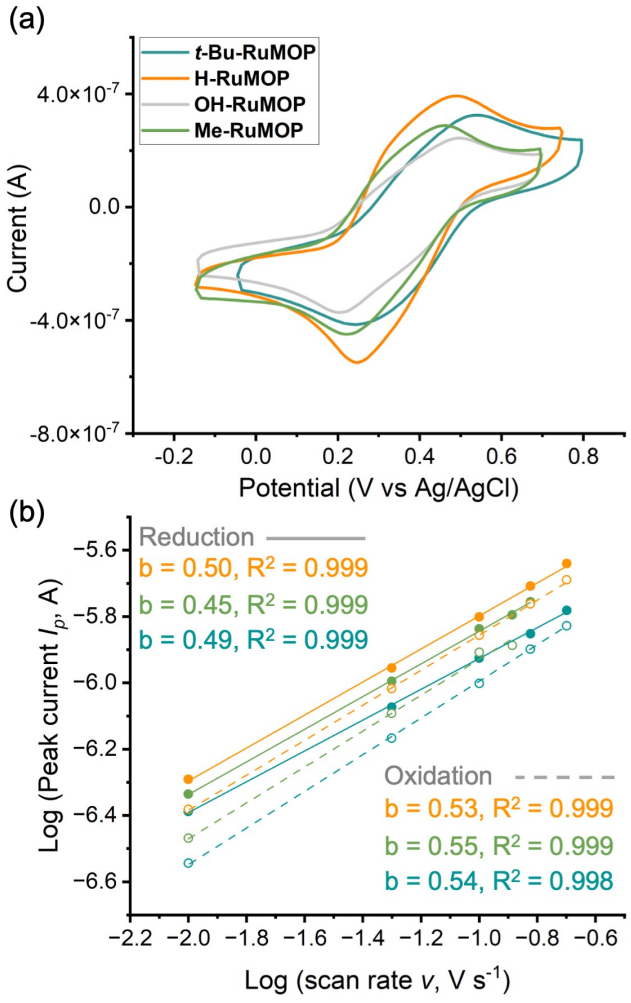

Figure 3. (a) CV of **H-RuMOP** (orange), **Me-RuMOP** (green), ***t*-Bu-RuMOP** (cyan), **OH-RuMOP** (gray). Voltammograms recorded in 0.1 M $[(n\text{-Bu})_4N][PF_6]$ DMF solution at υ = 10 mV s^{-1} with a glassy carbon working electrode, a platinum counter electrode and an Ag/AgCl reference electrode. (b) Logisim of the peak current I_p as a function of the Logisim of scan rate v. The value of b represents the slope of the curve. The solid circles are reduction processes, and the open circles are oxidation processes. The solid line is the linear fitting curve of the reduction process, and the dashed line is the linear fitting curve of the oxidation process.

Electrochemical properties of RuMOPs. The **H-RuMOP**, **Me-RuMOP** and ***t*-Bu-RuMOP** were expected to exhibit reversible redox activity due to the presence of mixvalance Ru_2(II/III) paddlewheels, which undergo reduction to the Ru_2(II/II) paddlewheel, and then return to the mixvalance state via oxidation. It has been reported that the redox process of the Ru-paddlewheel is influenced by changes in the electron density at equatorial carboxylates caused by functional group substitution.[36] To examine the effect of the functional group on the redox property of RuMOP, cyclic voltammetry (CV) of these three RuMOPs was performed (Figure S17). For further comparison, we also included **OH-RuMOP**.

The CV measurements were carried out versus Ag/AgCl counter electrode in DMF with 0.1 M $[(n\text{-Bu})_4N][PF_6]$ serving as the supporting electrolyte. Figure 3a indicates that the **H-RuMOP** displays distinct reduction (E_{pc}) and oxidation peaks (E_{pa}) at 0.248 and 0.492 V, respectively. The peak-to-peak separation (ΔE_p) is 0.254 V, and the half-wave potential ($E_{1/2}$, $E_{1/2} = (E_{pa} + E_{pc})/2$) is determined to be 0.370 V. The presence of the methyl groups shifted the reduction and oxidation potentials of **Me-RuMOP** to more negative region (0.226 V and 0.464 V, respectively), resulting in an $E_{1/2}$ value of 0.345 V, which is 0.025 V negatively shifted with respect to **H-RuMOP**. In contrast, ***t*-Bu-RuMOP** exhibits a substantial variation in $E_{1/2}$, with a value of 0.390 V, representing a significant positive shift of +0.020 V from **H-RuMOP**. In the case of **OH-RuMOP**, both the reduction (0.202 V) and the oxidation potential (0.498 V) have shifted to a more negative region, resulting in an $E_{1/2}$ of 0.350 V. When compared with **H-RuMOP**, the difference of $E_{1/2}$ is -0.020 V, which is similar to **Me-RuMOP**.

Depending on the negative or positive shift of $E_{1/2}$ compared to the $E_{1/2}$ of **H-RuMOP**, the functional groups of RuMOPs were classified into two categories: electron-donating groups and electron-withdrawing groups, respectively. The electron-donating groups were the methyl and hydroxy groups, which aligns with the Hammett constants[37] and previous research.[36] As a result, **Me-RuMOP** and **OH-RuMOP** are more difficult to be reduced. In the case of the *tert*-butyl group, it is an electron-donating group according to its Hammett constant of -0.1. However, it exhibits an electron-withdrawing effect, which was previously found in the *tert*-butyl group with hyperconjugation.[38] As a result, ***t*-Bu-RuMOP** can be easily reduced.

To determine whether the redox process of RuMOP was controlled by diffusion (faradaic process) or adsorption (capacitive process), CV with different scan rates were measured. The results were analyzed according to the relationship between the peak current (I_p) and the scan rate (v):

$$I_p = av^b \quad (1)$$

The value of b was determined by examining the slope of the log(v)-log(I) plot. Specifically, if b = 0.5, it indicates that the redox reactions are diffusion-controlled, whereas if b = 1.0, it indicates that the redox reactions are adsorption-controlled.[39] In all cases, both the anodic peak current

(I_{pa}) and cathodic peak current (I_{pc}) increased proportionally with increasing the scan rate from 10 mV s^{-1} to 200 mV s^{-1}. The *b* value of all RuMOPs is approximately 0.5 (Figure 3b), suggesting the dominance of the diffusion-controlled process, where the reaction rate equals the transport rate of RuMOP to the electrode in solution.

To elucidate the number of Ru-paddlewheels participating in the redox process, chronoamperometry measurements of **H-RuMOP** were conducted. The chronoamperometry was made through the potential step from 0.7 V to various values of potential ranging from 0.6 V to 0.0 V and the current was recorded in the time domain from 0.1 s to 21 s after stepping the potential. The linearity of the Cottrell plot was poor over the whole time-domain. When the background current was subtracted, the Cottrell plot showed an approximately linear relation in the time domain from 1.0 s to 3.0 s, in which the slope *S* of the plots was extracted by linear fitting and used for the following analysis. (Figure S18-S20) To estimate the number of transferred electrons, the Cottrell equation was employed:

$$i = \frac{nFAc^*\sqrt{D}}{\sqrt{\pi t}} \quad (2)$$

where *i* is the current, *n* is the number of electrons from one molecule of the analyte, *F* is the Faraday constant, *A* is the area of the planar electrode, c^* is the initial concentration of the reducible analyte, *D* is the diffusion coefficient for the analyte and *t* is time. By plugging the slope of the Cottrell plot *S* as $it^{-\frac{1}{2}}$ and the formula for the area of a circle into the Cottrell equation, it was rewritten as:

$$S = \pi^{\frac{1}{2}} F D^{\frac{1}{2}} r^2 c^* n \quad (3)$$

where *r* is the radius of the planar working electrode used. Here, we used a 1.5 mm planar working electrode, which was a suitable value for measuring chronoamperometry and computing the transferred electrons with the Cottrell equation.[40,41] Ferrocene oxidation was used as a standard redox reaction in this measurement (Figure S18-S19). The hydrodynamic diameters obtained through DLS measurement were employed to determine the diffusion coefficient *D* of **H-RuMOP** using the Stokes-Einstein equation (Equation S1), which yields a value of 1.89×10^{-10} m^2 s^{-1}. This value falls within the range previously reported for supramolecular cage materials.[42] The concentration c^* is the concentration of initial **H-RuMOP** solution and was used to estimate the number of transferred electrons during the reduction process.

As a result, the number of transferred electrons *n* per **H-RuMOP** molecule has been estimated as shown in Figure 4. During the reduction process of **H-RuMOP**, electron transfer did not occur above 0.5 V. Subsequently, when the potential decreases to the diffusion-controlled portion 0.2 – 0.0 V, the **H-RuMOP** exhibits a multi-electron transfer with the estimated number of 9 ± 0.8. This result indicates that during the reduction process, nine out of twelve redox sites in **H-RuMOP** were reduced. The incomplete redox reaction might be explained by the size of **H-RuMOP** over 2 nm; the redox site farthest from the electrode cannot be reduced by the electron transfer process. However, this result is sufficient to demonstrate the existence of a multi-electron transfer process.

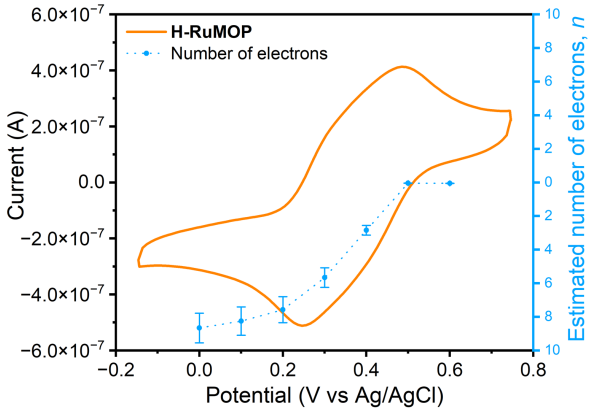

Figure 4. CV (orange) and estimated number of transferred electron (blue) of **H-RuMOP**. Transferred electrons were calculated from chronoamperometry measurements with the Cottrell equation, error bar represents the propagation of error (Equation S2). Chronoamperometry was recorded through the potential step from 0.7 V to various values of potential ranging from 0.6 V to 0.0 V.

Conclusion

In summary, three novel redox-active and permanently porous cuboctahedral RuMOPs based on Ru_2(II/III)-paddlewheel have been synthesized. The surface functionality of RuMOPs affects their properties in both the solution and the solid state. The **H-RuMOP** and **Me-RuMOP** were packed in body-centered cubic (bcc) arrangements, while ***t*-Bu-RuMOP** was packed in a face-centered cubic (fcc) arrangement. This difference is ascribed to the steric hindrance and the van der Waals interaction of the *tert*-butyl groups. Such interaction assists in the partial maintenance of crystallinity during activation at 120°C, resulting in higher N_2 uptake per cage of ***t*-Bu-RuMOP** than **H-RuMOP** and **Me-RuMOP**. The electrochemical measurements revealed that the functional group on R-bdc in RuMOPs influenced their redox potentials, **Me-RuMOP** and **OH-RuMOP** are negatively shifted and ***t*-Bu-RuMOP** is positively shifted, compared to **H-RuMOP**. The multi-electron transferred redox process of **H-RuMOP** was confirmed to involve approximately nine electrons in the reduction process. This study displays a strategy for designing multi-electron transfer materials by merging several redox-active sites into supramolecular structures. We envision that by regulating the quantity of redox-active sites, the number of electrons transferred can be controlled. This strategy holds promise for enhancing catalytic performance and generating mixed oxidized/reduced states synchronized with porous properties.

Experimental section

Materials and reagents All reagents were commercially sourced and used without further purification. The precursor $[Ru_2(OAc)_4(THF)_2](BF_4)$ and the $[Ru_2(OH\text{-}bdc)_2]_{12}(BF_4)_{12}$ **(OH-RuMOP)** was prepared by following a reported method.[26,43]

Synthesis of $[Ru_2(H\text{-}bdc)_2]_{12}(BF_4)_{12}$ (H-RuMOP). $[Ru_2(OAc)_4(THF)_2](BF_4)$ (0.180 g, 0.27 mmol) and benzene-1,3-dicarboxylic acid (0.170 g, 1.0 mmol) were dissolved in 2 mL of DMA. Then Na_2CO_3 (0.020 g, 0.19 mmol) was added. The solution was sealed in a vial and heated to 120 °C. After heating for 16 hours, brown single crystals of **H-RuMOP** were obtained. The product was then centrifuged and washed with DMA, water and methanol. The precipitate was suspended in approximately 4 mL of methanol, followed by the addition of 200 µL of aqueous HBF_4 (50 wt. %). The mixture was subsequently centrifuged, and the dark supernatant was discarded. The resulting yellowish-brown solids were dissolved in DMF and then poured into diethyl ether, yielding the precipitation of the yellowish-brown **H-RuMOP** solid. After centrifugation, the precipitates were washed with diethyl ether and dried at ambient conditions (yielding 83%).

Synthesis of $[Ru_2(Me\text{-}bdc)_2]_{12}(BF_4)_{12}$ (Me-RuMOP). $[Ru_2(OAc)_4(THF)_2](BF_4)$ (0.090 g, 0.135 mmol) and 5-methylbenzene-1,3-dicarboxylic acid (0.090 g, 0.5 mmol) were dissolved in 4 mL of DMA. Then Na_2CO_3 (0.020 g, 0.19 mmol) was added. The solution was sealed in a vial and heated to 120 °C. After heating for 20 hours, brown single crystals of **Me-RuMOP** were obtained. The product was centrifuged, and the resulting solid was subsequently washed with DMA, water and methanol. The precipitate was suspended in approximately 4 mL of methanoll and 200 µL of aqueous HBF_4 (50 wt. %) was added. The mixture was then centrifuged and the dark supernatant was discarded. The resulting yellowish-brown solids were dissolved in acetone and then poured into diethyl ether, yielding the precipitation of the yellowish-brown **Me-RuMOP** solid. After centrifugation, the precipitates were washed with diethyl ether and dried at ambient conditions (yielding 74%).

Synthesis of $[Ru_2(t\text{-}Bu\text{-}bdc)_2]_{12}(BF_4)_{12}$ (*t*-Bu-RuMOP). $[Ru_2(OAc)_4(THF)_2]BF_4$ (0.180 g, 0.27 mmol) and 5-*tert*-butylbenzene-1,3-dicarboxylic acid (0.020 g, 0.18 mmol) were dissolved in 1 mL of DMA. Then Na_2CO_3 (0.020 g, 0.19 mmol) was added. The solution was sealed in a vial and heated to 120 °C. After heating for 16 hours, brown single crystals of ***t*-Bu-RuMOP** were obtained. The product was centrifuged, and the resulting solid was subsequently washed with DMA, water and methanol. The solids were suspended in the minimal amount of methanol and 200 µL of aqueous HBF_4 (50 wt. %) was added. The mixture was then centrifuged and the dark supernatant was discarded. The resulting yellowish-brown solids were dissolved in acetone and then poured into diethyl ether, yielding the precipitation of the yellowish-brown ***t*-Bu-RuMOP** solid. After centrifugation, the precipitates were washed with diethyl ether and dried at ambient conditions (yielding 43%).

Physical characterization. Fourier-transform infrared (FT-IR) spectroscopy data were recorded using a Jasco FT/IR-6100. Powder X-ray diffraction (PXRD) data was collected using a Rigaku SmartLab diffractometer with Cu Kα radiation (λ = 1.54056 Å) in Bragg-Brentano geometry. Dynamic Light Scattering (DLS) and zeta potential measurements were performed using a Zetasizer Nano ZS (Malvern Instruments).

N_2 (77 K) gas sorption measurements. Gas sorption isotherms of were recorded on a BELSORP-mini-X volumetric adsorption instrument from BEL Japan Inc. Prior to gas sorption measurements the samples were activated at 120° C for 12 h.

Electrochemical measurements. Cyclic voltammograms (CV) and chronoamperometry were recorded on a CHI420 electrochemistry workstation with 3 electrode systems. Measurements were performed using a glassy carbon disk working electrode, a platinum counter electrode and an Ag/AgCl reference electrode. The working electrode radius was 1.5 mm and was polished with 0.05 um alumina before each run. The solution was purged with argon for 10 minutes and the measurements were conducted under an argon atmosphere. The electrolyte was 0.1 M DMF solution of $[(n\text{-}Bu)_4N][PF_6]$. For both CV and chronoamperometry of RuMOP, the concentration was 0.042 mM.

X-ray crystallographic analysis. Single crystal X-ray diffraction data for **H-RuMOP** was obtained by the synchrotron radiation (λ = 0.8097 Å) at the BL40XU beamline in the Super Photon ring-8 (SPring-8), Japan. Single crystal X-ray diffraction data for **Me-RuMOP** was obtained by the synchrotron radiation (λ = 0.4139 Å) at the BL02B1 beamline in the SPring-8. Single crystal X-ray diffraction data for ***t*-Bu-RuMOP** was obtained on a Rigaku model XtaLAB P200 diffractometer equipped with a Dectris model PILATUS 200K detector and confocal monochromatic Mo Kα radiation (λ = 0.71073 Å). The structure solution and refinement were performed using ShelXT[44] and ShelXL[45] using Least Squares minimization, operated through the Olex2[46] interface. The coordinated DMA molecules were refined isotopically. In consideration of single crystal analysis, oxygen atoms were placed at the axial positions of Ru-paddlewheels where coordinating solvent could not be explicitly modeled. For the refinements of the disordered *tert*-butyl group in the ***t*-Bu-RuMOP**, the *tert*-butyl group was divided into two sites related by the C-C bond rotation with the sum of the occupancies set as unity.

ASSOCIATED CONTENT

Supporting Information.
This Supporting Information is available free of charge via the Internet at http://xxxxx/doi/xxxxxxxxxx

Accession Codes
CCDC 2314398-2314400 contains the supplementary crystallographic data for this paper. These data can be obtained free of charge via www.ccdc.cam.ac.uk/data_request/cif, or by emailing data_request@ccdc.cam.ac.uk, or by contacting the

Cambridge Crystallographic Data Center, 12 Union Road, Cambridge CB12 1EZ UK; fax: +44 1223 336033.

AUTHOR INFORMATION

Corresponding Author

*__Shuhei Furukawa__ – Institute for Integrated Cell-Material Sciences (iCeMS), Kyoto University, Yoshida, Sakyo-ku, Kyoto 606-8501, Japan; Department of Synthetic Chemistry and Biological Chemistry, Graduate School of Engineering, Kyoto University, Katsura, Nishikyo-ku, Kyoto 615-8510, Japan; orcid.org/0000-0003-3849-8038; Email: shuhei.furukawa@icems.kyoto-u.ac.jp

Authors

Fuerkaiti Tayier – Institute for Integrated Cell-Material Sciences (iCeMS), Kyoto University, Yoshida, Sakyo-ku, Kyoto 606-8501, Japan; Department of Synthetic Chemistry and Biological Chemistry, Graduate School of Engineering, Kyoto University, Katsura, Nishikyo-ku, Kyoto 615-8510, Japan; orcid.org/0009-0000-1349-6752.

Javier Troyano – Institute for Integrated Cell-Material Sciences (iCeMS), Kyoto University, Yoshida, Sakyo-ku, Kyoto 606-8501, Japan; Department of Inorganic Chemistry, Autonomous University of Madrid, 28049 Madrid, Spain. Institute for Advanced Research in Chemical Sciences (IAdChem), Autonomous University of Madrid, 28049 Madrid, Spain*; orcid.org*/0000-0002-0213-8148.

Shun Tokuda – Institute for Integrated Cell-Material Sciences (iCeMS), Kyoto University, Yoshida, Sakyo-ku, Kyoto 606-8501, Japan; Department of Synthetic Chemistry and Biological Chemistry, Graduate School of Engineering, Kyoto University, Katsura, Nishikyo-ku, Kyoto 615-8510, Japan.

Zaoming Wang – Institute for Integrated Cell-Material Sciences (iCeMS), Kyoto University, Yoshida, Sakyo-ku, Kyoto 606-8501, Japan; Japan*; orcid.org*/0009-0003-1385-8164;

Masa-aki Haga –Research & Development Initiative, Chuo University, 1-13-27 Kasuga, Bunkyo-ku, Tokyo 112-8551, Japan.

Author Contributions

The manuscript was written through the contributions of all authors. All authors have given approval to the final version of the manuscript.

Notes

The authors declare no competing financial interest.

ACKNOWLEDGMENT

F. T. acknowledges the support of the Japan Science and Technology Agency (JST), the establishment of university fellowship towards the creation of science technology innovation, Grant Number JPMJFS2123. This work was supported by JSPS KAKENHI grant number 21K18192 (Challenging Research (Pioneering)) and 23H00298 (Kiban A) for S. F. The authors thank the iCeMS Analysis Centre for access to analytical instruments. The synchrotron radiation experiments for **H-RuMOP** single crystal structural analysis were performed at the BL40XU of SPring-8 with the approval of the Japan Synchrotron Radiation Research Institute (JASRI) (Proposal No. 2023A1747). The synchrotron radiation experiments for **Me-RuMOP** single crystal structural analysis were performed at the BL02B1 of SPring-8 with the approval of the Japan Synchrotron Radiation Research Institute (JASRI) (Proposal No. 2023B1307).

REFERENCES

1. De Santis, G.; Fabbrizzi, L.; Licchelli, M.; Pallavicini, P. Redox process in supramolecular coordination compounds. *Coord. Chem. Rev.* **1992**, 120, 237-257. DOI: 10.1016/0010-8545(92)80054-U
2. Shukla, J.; Singh, V. P.; Mukhopadhyay, P. Molecular and Supramolecular Multiredox Systems. *ChemistryOpen* **2020**, *9* (3), 304–324. DOI: 10.1002/open.201900339.
3. Peng, C.; Ning, G.-H.; Su, J.; Zhong, G.; Tang, W.; Tian, B.; Su, C.; Yu, D.; Zu, L.; Yang, J.; Ng, M.-F.; Hu, Y.-S.; Yang, Y.; Armand, M.; Loh, K. P. Reversible Multi-Electron Redox Chemistry of π-Conjugated N-Containing Heteroaromatic Molecule-Based Organic Cathodes. *Nature Energy* **2017**, 2 (7), 1–9. DOI: 10.1038/nenergy.2017.74.
4. Chen, R.; Luo, R.; Huang, Y.; Wu, F.; Li, L. Advanced High Energy Density Secondary Batteries with Multi-Electron Reaction Materials. *Adv. Sci.* **2016**, *3* (10), 1600051. DOI: 10.1002/advs.201600051.
5. Gersten, S. W.; Samules, G. J.; Meyer, T. J. Catalytic Oxidation of Water by an Oxo-Bridged. *J. Am. Chem. Soc*. **1982**, 104(14), 4029-4030. DOI: 10.1021/ja00378a053
6. Bessinger, D.; Muggli, K.; Beetz, M.; Auras, F.; Bein, T. Fast-Switching Vis-IR Electrochromic Covalent Organic Frameworks. *J. Am. Chem. Soc.* **2021**, *143* (19), 7351–7357. DOI: 10.1021/jacs.0c12392.
7. Sun, J.; Wu, Y.; Wang, Y.; Liu, Z.; Cheng, C.; Hartlieb, K. J.; Wasielewski, M. R.; Stoddart, J. F. An Electrochromic Tristable Molecular Switch. *J. Am. Chem. Soc.* **2015**, *137* (42), 13484–13487. DOI: 10.1021/jacs.5b09274.
8. Zhang, Z.; Huang, L.; Shulmeister, V. M.; Chi, Y. I.; Kim, K. K.; Hung, L. W.; Crofts, A. R.; Berry, E. A.; Kim, S. H. Electron Transfer by Domain Movement in Cytochrome bc1. *Nature* **1998**, *392* (6677), 677–684. DOI: 10.1038/33612.
9. Eddaoudi, M.; Kim, J.; Wachter, J. B.; Chae, H. K.; O'Keeffe, M.; Yaghi, O. M. Porous Metal-Organic Polyhedra: 25 A Cuboctahedron Constructed from 12 Cu2(CO2)4 Paddle-Wheel Building Blocks. *J. Am. Chem. Soc.* **2001**, *123* (18), 4368–4369. DOI: 10.1021/ja0104352.
10. Gosselin, A. J.; Rowland, C. A.; Bloch, E. D. Permanently Microporous Metal-Organic Polyhedra. *Chem. Rev.* **2020**, *120* (16), 8987–9014. DOI: 10.1021/acs.chemrev.9b00803.
11. Zhang, D.; Ronson, T. K.; Zou, Y.-Q.; Nitschke, J. R. Metal–organic Cages for Molecular Separations. *Nature Reviews Chemistry* **2021**, *5* (3), 168–182. DOI: 10.1038/s41570-020-00246-1.
12. Ahmad, N.; Younus, H. A.; Chughtai, A. H.; Verpoort, F. Metal-Organic Molecular Cages: Applications of Biochemical Implications. *Chem. Soc. Rev.* **2015**, *44* (1), 9–25. DOI: 10.1039/c4cs00222a.
13. Li, J.-R.; Zhou, H.-C. Bridging-Ligand-Substitution Strategy for the Preparation of Metal-Organic Polyhedra. *Nat. Chem.* **2010**, *2* (10), 893–898. DOI: 10.1038/nchem.803.
14. Carné-Sánchez, A.; Albalad, J.; Grancha, T.; Imaz, I.; Juanhuix, J.; Larpent, P.; Furukawa, S.; Maspoch, D. Postsynthetic Covalent and Coordination Functionalization of Rhodium(II)-Based Metal-Organic Polyhedra. *J. Am. Chem. Soc.* **2019**, *141* (9), DOI: 10.1021/jacs.8b13593.
15. Albalad, J.; Hernández-López, L.; Carné-Sánchez, A.; Maspoch, D. Surface Chemistry of Metal-Organic

Polyhedra. *Chem. Commun.* **2022**, *58* (15), 2443–2454. DOI: 10.1039/d1cc07034g.
16. Furutani, Y.; Kandori, H.; Kawano, M.; Nakabayashi, K.; Yoshizawa, M.; Fujita, M. In Situ Spectroscopic, Electrochemical, and Theoretical Studies of the Photoinduced Host-Guest Electron Transfer That Precedes Unusual Host-Mediated Alkane Photooxidation. *J. Am. Chem. Soc.* **2009**, *131* (13), 4764–4768. DOI: 10.1021/ja8089075.
17. Li, Y.-H.; Jiang, J.-J.; Fan, Y.-Z.; Wei, Z.-W.; Chen, C.-X.; Yu, H.-J.; Zheng, S.-P.; Fenske, D.; Su, C.-Y.; Barboiu, M. Solvent- and Anion-Induced Interconversions of Metal-Organic Cages. *Chem. Commun.* **2016**, *52* (56), 8745–8748. DOI: 10.1039/c6cc04420d.
18. Lu, Y.-L.; Song, J.-Q.; Qin, Y.-H.; Guo, J.; Huang, Y.-H.; Zhang, X.-D.; Pan, M.; Su, C.-Y. A Redox-Active Supramolecular Fe4L6 Cage Based on Organic Vertices with Acid-Base-Dependent Charge Tunability for Dehydrogenation Catalysis. *J. Am. Chem. Soc.* **2022**, *144* (19), 8778–8788. DOI: 10.1021/jacs.2c02692.
19. Cai, L.-X.; Li, S.-C.; Yan, D.-N.; Zhou, L.-P.; Guo, F.; Sun, Q.-F. Water-Soluble Redox-Active Cage Hosting Polyoxometalates for Selective Desulfurization Catalysis. *J. Am. Chem. Soc.* **2018**, *140* (14), 4869–4876. DOI: 10.1021/jacs.8b00394.
20. Plessius, R.; Orth, N.; Ivanović-Burmazović, I.; Siegler, M. A.; Reek, J. N. H.; van der Vlugt, J. I. Reversible Multi-Electron Storage in Dual-Site Redox-Active Supramolecular Cages. *Chem. Commun.* **2019**, *55* (84), 12619–12622. DOI: 10.1039/c9cc07138e.
21. Vasdev, R. A. S.; Findlay, J. A.; Garden, A. L.; Crowley, J. D. Redox Active $[Pd_2L_4]^{4+}$ Cages Constructed from Rotationally Flexible 1,1′-Disubstituted Ferrocene Ligands. *Chem. Commun.* **2019**, *55* (52), 7506–7509. DOI: 10.1039/C9CC03321A.
22. Li, K.; Zhang, L.-Y.; Yan, C.; Wei, S.-C.; Pan, M.; Zhang, L.; Su, C.-Y. Stepwise Assembly of $Pd_{(6)}(RuL_{(3)})(8)$ Nanoscale Rhombododecahedral Metal-Organic Cages via Metalloligand Strategy for Guest Trapping and Protection. *J. Am. Chem. Soc.* **2014**, *136* (12), 4456–4459. DOI: 10.1021/ja410044r.
23. Mahata, K.; Frischmann, P. D.; Würthner, F. Giant Electroactive M4L6 Tetrahedral Host Self-Assembled with Fe(II) Vertices and Perylene Bisimide Dye Edges. *J. Am. Chem. Soc.* **2013**, *135* (41), 15656–15661. DOI: 10.1021/ja4083039.
24. Glatz, J.; Donnart, M.; Gontard, G.; Li, Y.; Lescouëzec, R. Design of Redox-Active Cs⊂{Fe4Ni4} Cyanide-Bridged Cage Complexes Bearing Monodentate Ligands: Synthesis, Structure, and Electronic Properties. *Cryst. Growth Des.* **2023**, *23* (3), 1709–1717. DOI: 10.1021/acs.cgd.2c01278.
25. Young, M. D.; Zhang, Q.; Zhou, H.-C. Metal–organic Polyhedra Constructed from Dinuclear Ruthenium Paddlewheels. *Inorganica Chim. Acta* **2015**, *424*, 216–220. DOI: 10.1016/j.ica.2014.09.010.
26. Troyano, J.; Tayier, F.; Phattharaphuti, P.; Aoyama, T.; Urayama, K.; Furukawa, S. Porous Supramolecular Gels Produced by Reversible Self-Gelation of Ruthenium-Based Metal-Organic Polyhedra. *Chem. Sci.* **2023**, *14* (35), 9543–9552. DOI: 10.1039/d3sc02888g.
27. Furukawa, S.; Horike, N.; Kondo, M.; Hijikata, Y.; Carné-Sánchez, A.; Larpent, P.; Louvain, N.; Diring, S.; Sato, H.; Matsuda, R.; Kawano, R.; Kitagawa, S. Rhodium-Organic Cuboctahedra as Porous Solids with Strong Binding Sites. *Inorg. Chem.* **2016**, *55* (21), 10843–10846. DOI : 10.1021/acs.inorgchem.6b02091.
28. Li, J.-R.; Yakovenko, A. A.; Lu, W.; Timmons, D. J.; Zhuang, W.; Yuan, D.; Zhou, H.-C. Ligand Bridging-Angle-Driven Assembly of Molecular Architectures Based on Quadruply Bonded Mo-Mo Dimers. *J. Am. Chem. Soc.* **2010**, 132 (49), 17599–17610. DOI: 10.1021/ja1080794.
29. Aquino, M. A. S. Diruthenium and Diosmium Tetracarboxylates: Synthesis, Physical Properties and Applications. *Coord. Chem. Rev.* **1998**, *170* (1), 141 – 202. DOI: 10.1016/S0010-8545(97)00079-9.
30. Holomb, R.; Martinelli, A.; Albinsson, I.; Lassègues, J. C.; Johansson, P.; Jacobsson, P. Ionic Liquid Structure: The Conformational Isomerism in 1-butyl-3-methyl-imidazolium Tetrafluoroborate ([bmim][BF_4]). *J. Raman Spectrosc.* **2008**, *39* (7), 793–805. DOI: 10.1002/jrs.1912.
31. Furukawa, S.; Kitagawa, S. Neutral Paddlewheel Diruthenium Complexes with Tetracarboxylates of Large Pi-Conjugated Substituents: Facile One-Pot Synthesis, Crystal Structures, and Electrochemical Studies. *Inorg. Chem.* **2004**, *43* (20), 6464–6472. DOI: 10.1021/ic0493752
32. Park, J.; Perry, Z.; Chen, Y.-P.; Bae, J.; Zhou, H.-C. Chromium(II) Metal-Organic Polyhedra as Highly Porous Materials. *ACS Appl. Mater. Interfaces* **2017**, *9* (33), 28064–28068. DOI: 10.1021/acsami.7b09339.
33. Barreda, O.; Bannwart, G.; Yap, G. P. A.; Bloch, E. D. Ligand-Based Phase Control in Porous Molecular Assemblies. *ACS Appl. Mater. Interfaces* **2018**, *10* (14), 11420–11424. DOI: 10.1021/acsami.8b02015.
34. Osterrieth, J. W. M.; Rampersad, J.; Madden, D.; Rampal, N.; Skoric, L.; Connolly, B.; Allendorf, M. D.; Stavila, V.; Snider, J. L.; Ameloot, R.; Marreiros, J.; Ania, C.; Azevedo, D.; Vilarrasa-Garcia, E.; Santos, B. F.; Bu, X.-H.; Chang, Z.; Bunzen, H.; Champness, N. R.; Griffin, S. L.; Chen, B.; Lin, R.-B.; Coasne, B.; Cohen, S.; Moreton, J. C.; Colón, Y. J.; Chen, L.; Clowes, R.; Coudert, F.-X.; Cui, Y.; Hou, B.; D'Alessandro, D. M.; Doheny, P. W.; Dincă, M.; Sun, C.; Doonan, C.; Huxley, M. T.; Evans, J. D.; Falcaro, P.; Ricco, R.; Farha, O.; Idrees, K. B.; Islamoglu, T.; Feng, P.; Yang, H.; Forgan, R. S.; Bara, D.; Furukawa, S.; Sanchez, E.; Gascon, J.; Telalović, S.; Ghosh, S. K.; Mukherjee, S.; Hill, M. R.; Sadiq, M. M.; Horcajada, P.; Salcedo-Abraira, P.; Kaneko, K.; Kukobat, R.; Kenvin, J.; Keskin, S.; Kitagawa, S.; Otake, K.-I.; Lively, R. P.; DeWitt, S. J. A.; Llewellyn, P.; Lotsch, B. V.; Emmerling, S. T.; Pütz, A. M.; Martí-Gastaldo, C.; Padial, N. M.; García-Martínez, J.; Linares, N.; Maspoch, D.; Suárez Del Pino, J. A.; Moghadam, P.; Oktavian, R.; Morris, R. E.; Wheatley, P. S.; Navarro, J.; Petit, C.; Danaci, D.; Rosseinsky, M. J.; Katsoulidis, A. P.; Schröder, M.; Han, X.; Yang, S.; Serre, C.; Mouchaham, G.; Sholl, D. S.; Thyagarajan, R.; Siderius, D.; Snurr, R. Q.; Goncalves, R. B.; Telfer, S.; Lee, S. J.; Ting, V. P.; Rowlandson, J. L.; Uemura, T.; Iiyuka, T.; van der Veen, M. A.; Rega, D.; Van Speybroeck, V.; Rogge, S. M. J.; Lamaire, A.; Walton, K. S.; Bingel, L. W.; Wuttke, S.; Andreo, J.; Yaghi, O.; Zhang, B.; Yavuz, C. T.; Nguyen, T. S.; Zamora, F.; Montoro, C.; Zhou, H.; Kirchon, A.; Fairen-Jimenez, D. How Reproducible Are Surface Areas Calculated from the BET Equation? *Adv. Mater.* **2022**, *34* (27), e2201502. DOI: 10.1002/adma.202201502.
35. Lorzing, G. R.; Gosselin, A. J.; Trump, B. A.; York, A. H. P.; Sturluson, A.; Rowland, C. A.; Yap, G. P. A.; Brown, C. M.; Simon, C. M.; Bloch, E. D. Understanding Gas Storage in Cuboctahedral Porous Coordination Cages. *J. Am. Chem. Soc.* **2019**, *141* (30), 12128–12138. DOI: 10.1021/jacs.9b05872.
36. Kosaka, W.; Watanabe, Y.; Itoh, C.; Miyasaka, H. High Stabilization of Low Valency in a Homoleptic Ortho-Hydroxybenzoate-Bridged Paddlewheel Diruthenium(II,II) Complex. *Chem. Lett.* **2022**, *51* (7), 731–734. DOI: 10.1246/cl.220195.

37. McDaniel, D. H.; Brown, H. C. An Extended Table of Hammett Substituent Constants Based on the Ionization of Substituted Benzoic Acids. *J. Org. Chem.* **1958**, 23(3), 420-427. DOI: 10.1021/jo01097a026
38. Zhou, P.; Aschauer, U.; Decurtins, S.; Feurer, T.; Häner, R.; Liu, S.-X. Effect of Tert-Butyl Groups on Electronic Communication between Redox Units in Tetrathiafulvalene-Tetraazapyrene Triads. *Chem. Commun.* **2021**, *57* (96), 12972–12975. DOI: 10.1039/d1cc05671a.
39. Henrik, L. m.; So, S.; Solbrand, A.; Rensmo, H.; Hjelm, J.; Hagfeldt, A.; Lindquist, S.-E. Li Ion Insertion in TiO (Anatase). 2. Voltammetry on Nanoporous Films. *J. Phys. Chem. B.* **1997**, 101(39), 7717-7722. DOI: 10.1021/jp970490q
40. Nishiumi, T.; Abdul, M.; Aoki, K. Determination of the Number of Electrons by Chronoamperometry at Small Electrodes. *Electrochem. commun.* **2005**, *7* (12), 1213–1217. DOI: 10.1016/j.elecom.2005.08.030.
41. Baranski, A. S.; Fawcett, W. R.; And, 1.; Gilbert, M. Use of microelectrodes for the rapid determination of the number of electrons involved in an electrode reaction. *Anal. Chem.* **1985**, 57(1), 166-170. DOI: 10.1021/ac00279a041.
42. McConnell, A. J. Metallosupramolecular Cages: From Design Principles and Characterisation Techniques to Applications. *Chem. Soc. Rev.* **2022**, 51 (8), 2957-2971. DOI: 10.1039/d1cs01143j.
43. Urbanos, F. A.; Barral, M. C.; JIMl, R. SYNTHESIS AND PROPERTIES OF SOME DIRUTHENIUM ACETATE COMPOUNDS. *Plan. Perspect.* **1988**, *2597*, 2600. DOI: 10.1016/S0277-5387(00)83879-6.
44. Sheldrick, G. M. SHELXT - Integrated Space-Group and Crystal-Structure Determination. *Acta Crystallogr A Found Adv* **2015**, *71* (Pt 1), 3–8. DOI: 10.1107/S2053273314026370.
45. Sheldrick, G. M. Crystal Structure Refinement with SHELXL. *Acta Crystallogr. B* **2015**, *71* (Pt 1), 3–8. DOI: 10.1107/S2053229614024218.
46. Dolomanov, O. V.; Bourhis, L. J.; Gildea, R. J.; Howard, J. A. K.; Puschmann, H. OLEX2: A Complete Structure Solution, Refinement and Analysis Program. *J. Appl. Crystallogr.* **2009**, *42* (2), 339–341. DOI: 10.1107/S0021889808042726.